ELSEVIER

Marine Geology 141 (1997) 157–181

MARINE GEOLOGY
INTERNATIONAL JOURNAL OF MARINE GEOLOGY, GEOCHEMISTRY AND GEOPHYSICS

Boundary layer dynamics and sediment transport under storm and non-storm conditions on the Scotian Shelf

Michael Z. Li *, Carl L. Amos, David E. Heffler

Geological Survey of Canada, Bedford Institute of Oceanography, Atlantic Geoscience Centre, 1 Challenger Drive, Dartmouth, NS B2Y 4A2, Canada

Received 15 January 1997; accepted 28 April 1997

Abstract

Near-bed measurements of waves, currents, seabed responses and ripple migration rates were obtained using an instrumented tripod at a water depth of 39 m on the Scotian Shelf during the winter of 1992/93. These data and the Grant and Madsen's (1986) [Grant, W.D., Madsen, O.S., 1986. The continental shelf bottom boundary layer. Annu. Rev. Fluid Mech. 18, 265–305.] combined-flow boundary layer model are used to examine wave–current interaction, various sediment dynamic thresholds and sediment transport on an exposed, high-energy continental shelf. The seabed was found to be rippled for most time of the deployment and thus the ripple-enhanced combined skin-friction shear velocity had to be used to determine the initiation of bedload transport under combined flows. This indirectly indicates adequate predictions of the skin-friction shear velocities inside the wave boundary layer by the Grant and Madsen model. At high transport stages, bedload roughness must be added to the grain size roughness to obtain a transport-related combined shear velocity in order to predict correctly the onsets of saltation/suspension and sheet flow transports. Otherwise, the initiation of suspended load transport and the total sediment transport rates will be severely under-estimated. The comparison between the prediction by the Grant and Madsen (1986) model and the calculation of a quadratic stress law suggests that the total current shear velocity was enhanced by a factor of 2–3 due to the wave–current interaction during storms, while the apparent bottom roughness was increased by more than an order of magnitude. The non-linear coupling between waves and currents also causes a 20% increase of the combined skin-friction shear velocity inside the wave boundary layer. This non-linear coupling is most important when waves and currents are roughly equal in magnitude and the angles between them are less than 30°. Four sediment transport formulae were tested. While the Engelund–Hansen total-load and Yalin bedload methods did not perform well, the Einstein–Brown and Bagnold formulae were found to, respectively, give reasonable predictions of the bedload and total-load sediment transport rates under the observed combined-flow conditions. The predicted sediment transport direction is also in good agreement with the observed ripple migration direction. The GSC sediment transport model SEDTRANS92 predicts that the net daily transport rates during the storms reached 822 kg m^{-1} day^{-1} and were 2–3 orders of magnitude higher than the non-storm transport, suggesting the dominance of storm processes in sediment transport on the Scotian Shelf. These values are in good agreement with the results from sand tracer experiments conducted in this region. We thus conclude that SEDTRANS92 can properly simulate boundary layer dynamics and sediment transport on continental shelves. © 1997 Elsevier Science B.V.

Keywords: continental shelf; combined waves and currents; bottom boundary layer dynamics; sediment transport thresholds; storm sediment transport

* Corresponding author. Phone: (902) 426-9459; fax: (902) 426-4104; e-mail: li@agc.bio.ns.ca

PII S0025-3227(97)00060-1

1. Introduction

Seabed responses to combined waves and currents differ from those to unidirectional flows. The bottom boundary layer (bbl) models developed by Smith (1977) and Grant and Madsen (1979) predict the enhanced wave and current shear stresses and the resultant near-bed velocity profiles in a combined flow. These models have been extended later to include effects of movable rough bed and suspended sediment stratification (Smith and McLean, 1977; Grant and Madsen, 1982; Glenn and Grant, 1987). Estimates of current shear velocities, u_{*c}, and apparent roughness length, z_{0c}, above the wave boundary layer using velocity profiles obtained from the California shelf (Grant et al., 1984; Cacchione et al., 1987; Drake and Cacchione, 1992) and the Nova Scotian Shelf (Huntley and Hazen, 1988) have verified certain aspects of these models. However, the experiments to date have been conducted either over mud-rich sediments which do not produce well-formed bedforms, or the physical bed roughness and its temporal variation were not well specified. Therefore field measurements of wave–current dynamics and seabed roughness in diverse shelf and nearshore environments are still required (Cacchione and Drake, 1990).

Since mean current shear stress above the wave boundary layer is determined by the physical bed roughness as well as wave–current interaction, the precise knowledge of the bedforms is important to model verification. As ripples are developed, they alter near-bed pressure gradients, cause flow separation and vortex shedding, and induce form drag. Recent studies have evaluated the effects of ripple formation on near-bed velocity profiles, skin friction/form drag partition, and sand resuspension (Vincent et al., 1991; Wiberg and Nelson, 1992; Li, 1994; Li et al., 1996). Geometries of wave ripples have been measured in numerous field and laboratory experiments (Inman, 1957; Carstens et al., 1969; Mogridge and Kamphuis, 1972; Dingler and Inman, 1976; Miller and Komar, 1980a,b; Boyd et al., 1988). Several predictors of wave-formed ripples have been proposed (Nielsen, 1981; Grant and Madsen, 1982; Mogridge et al., 1994; Wiberg and Harris, 1994). However, few papers report the formation and geometry of ripples under combined waves and currents (Amos et al., 1988; Arnott and Southard, 1990). Sediment transport can be accurately predicted only if threshold criteria can be properly defined for the various phases of sediment transport (bedload traction, saltation/suspension and sheet flow). Although these thresholds are reasonably established for pure waves and pure unidirectional flows (Bagnold, 1956; Komar and Miller, 1975a,b; Madsen and Grant, 1975; Miller et al., 1977; Yalin and Karahan, 1979), solutions and field data for combined flows are limited (Hammond and Collins, 1979; Amos et al., 1988; Kapdasli, 1990). The sheet flow threshold for combined flows is unknown due to the greater difficulty of observation in the field.

Bedload transport takes place only within a few grain diameters of the bed, so no instrument is available to accurately measure bedload in the field. Yet bedload transport is a part of the total load transport and can be significant when coarse-grained sediment or large bedforms are involved. Tracer sand and ripple migration measurements have been used to quantify bedload transport and to test various predictive models in the marine environment (Lees, 1983; Heathershaw, 1981; Sternberg, 1972; Amos et al., 1997), but more field measurements of bedload transport under complex combined flows are needed.

An instrumented tripod (RALPH) was deployed on Sable Island Bank, Scotian Shelf in 39 m of water during the winter of 1992/1993 to monitor near-bed wave–current dynamics and seabed responses over well-sorted, medium sand. As RALPH measured currents at only two heights, we cannot test combined-flow bbl models, but rather our first objective is to provide needed field measurements of waves, current and associated seabed responses over a medium sand bed in a wide range of relative wave and current strengths. Estimates of bed stress from the combined-flow model of Grant and Madsen (1986, hereafter GM86) are compared to calculations using the quadratic stress law to quantify the enhancement of bottom shear stresses due to the non-linear interaction between waves and currents. Nearly 700 seabed photographs were taken by RALPH to successfully capture various seabed states, ranging from no transport, through active ripple and saltation/suspension, to sheet flows. Thus the second objective of this paper is to correlate these observed bed states with wave–current data to define the threshold criteria for various sediment transport phases under combined-flow conditions. The generation and classification of ripples, their dynamic transition and bed roughness predictions are presented in separate publications. It is well known that storm processes dominate sediment transport on continental shelves (Smith and Hopkins, 1972; Butman et al., 1979; Swift et al., 1986a,b), but the magnitude and direction of storm transport are not well known. So the third objective of this study is to utilize the available ripple migration rate measurements from Sable Island Bank to evaluate the applicability of various existing sediment transport formulae to combined flows and to simulate sand transport in storms.

2. Field method and data analysis

2.1. Study site and instrumentation

Sable Island Bank is located about 150 km off the southeast coast of Nova Scotia (Fig. 1), on the east coast of Canada. It is underlain by approximately 20 m of well-sorted Holocene sand, moulded into a series of shoreface-connected sand ridges. Tidal currents are semidiurnal ellipses rotating 360° in a clockwise direction over a tidal cycle. Peak tidal flows reach 0.35 m/s and are strongly anisotropic (northeast to southwest). Waves generally come from the south and southwest due to the sheltering by Sable Island to the north. Peak significant wave heights and mean wave periods can reach 6–8 m and 10–13 s, respectively, during the winter months (December to February), while the summer significant wave heights are less than 2 m. Detailed reviews of the physical oceanography and surficial geology can be found in Mobil Oil Canada Ltd. (1983) and Amos et al. (1988).

The instrumented tripod RALPH (Heffler, 1984) was deployed at site 1 on Sable Island Bank (Fig. 1) from January 17 to February 14, 1993. The tripod measured oscillatory and steady flows, hydrostatic pressure, and near-bed suspended sediment concentration. The water depth at the study site was 39 m and bottom sediment was composed of well-sorted medium quartz sand with a mean grain size $D=0.34$ mm. RALPH was equipped with two SACM acoustic current meters at 0.5 and 1.0 m above the bed, a Viatran 218-12 (250 psi) pressure transducer at 1.5 m above the base, two SeaTech optical transmissometers at 0.3 and 0.7 m and a KVH c-100 flux gate compass mounted at a height of 1.4 m. A Minolta 601 super-8 movie camera was mounted at 1.5 m with a flash at 0.55 m from the seabed. The nodal line of the camera was 20° from the vertical to give a field of view of 1.0 × 1.5 m in size. A shadow bar was also installed (0.17 m above the bed and 0.45 m outward away from the vertical of the flash) for ripple height and wavelength measurements. The system was controlled by an Onset computer and data were recorded on an Onset TattleTale Model 6 data logger with a 20 Mbyte hard disk. For this study, RALPH was programmed to sample all the sensors every 2 h for 18 min at a frequency of 1 Hz. Two seabed photographs were taken 15 min apart for each sampling burst to monitor seabed responses. The current meters were calibrated in a towing tank before the deployment, but the transmissometers were not calibrated and thus transmission percentages will be used here as a qualitative measure of the suspended sediment concentration.

2.2. Data analysis

For each time series, the following burst-average parameters were first obtained: mean water depth, h, mean current velocity 1 m above the bed, u_{100}, mean current direction, C_{dir}, and mean suspended sediment concentration (as % transmission) at 0.7 m above the bed, SSC1. The depth–time series was de-meaned to obtain the wave height record which was used to compute the wave energy density spectrum. Wave period, T, was estimated from the peak of this spectrum and the significant wave height was obtained from

$$H_s = 4M_0^{0.5} \quad (1)$$

where M_0 is the first moment (area under the

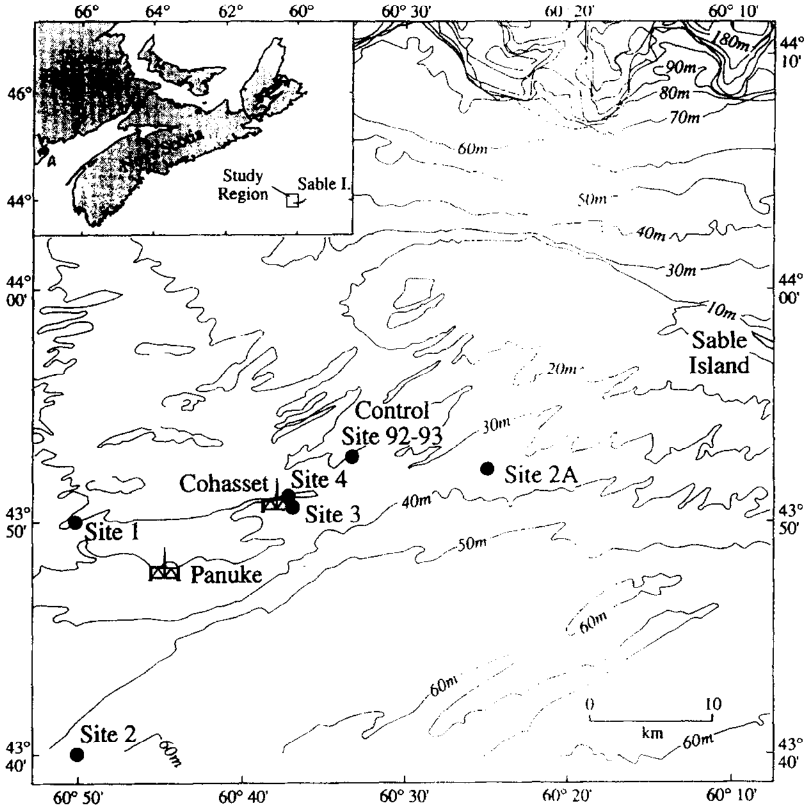

Fig. 1. The location map showing the study region on Sable Island Bank, Scotian Shelf.

spectrum) of the wave energy density spectrum. For each velocity–time series, the mean value was removed and the $u-v$ components of the maximum orbital velocities were plotted and the mean wave direction, W_{dir}, was then determined by a linear least-squares fit to this scatter diagram. The burst average depth h, mean current velocity u_{100}, significant wave height H_s, peak spectral wave period T, mean sediment diameter D and the acute angle between waves and currents were then used as input to the GM86 combined-flow bottom boundary layer model to compute current shear velocity, u_{*cs}, wave shear velocity, u_{*ws}, combined wave–current shear velocity, u_{*cws} (s in the subscript here denotes the skin-friction component), wave boundary layer height, δ_{cw}, apparent bottom roughness above the wave boundary layer, z_{0c}, and other bbl parameters for further data analysis.

The RALPH images were digitized using a computer-controlled film advancing system, a photo enlarger and a Sony video camera. The photo enlarger projected each frame directly onto the CCD of the video camera and the video signal was digitized using a Matrox frame-grabber in a PC. The digitized images were then analyzed using the Geographical Resources Assessment (GRASS) software package for seabed state classification, ripple geometry and ripple migration rate measurements. For each image, ripple wavelength, λ, was directly measured by referencing to the scales on the shadow bar. Ripple height, η, was calculated by knowing the light–shadow bar geometry and measuring the horizontal distances between the shadow and shadow bar for the ripple crest and trough, respectively. The ripple crest lines were traced (digitized) in GRASS and each pair of these digitized vector files was overlain to obtain the ripple migration rate, R_m. If the measured ripple migration rate was smaller than the GRASS digitization resolution (0.1 mm/min), *no motion* was defined as the bed state. If seabed images were clear and $R_m \geq 0.1$ mm/min, *bedload transport* would be classified. Observation of sand clouds and the general deterioration of image clarity marked the initiation of *saltation/suspension*, while the combination of strong image blurring and clearly recognized flat bed would indicate the upper-plane bed *sheet flow* condition.

3. Results

3.1. Overview of data

Fig. 2 shows the time series of (a) the burst-averaged water depth, h, (b) mean velocity at 1 m above the seabed, u_{100}, (c) significant wave height, H_s and spectral peak wave period, T, and (d)

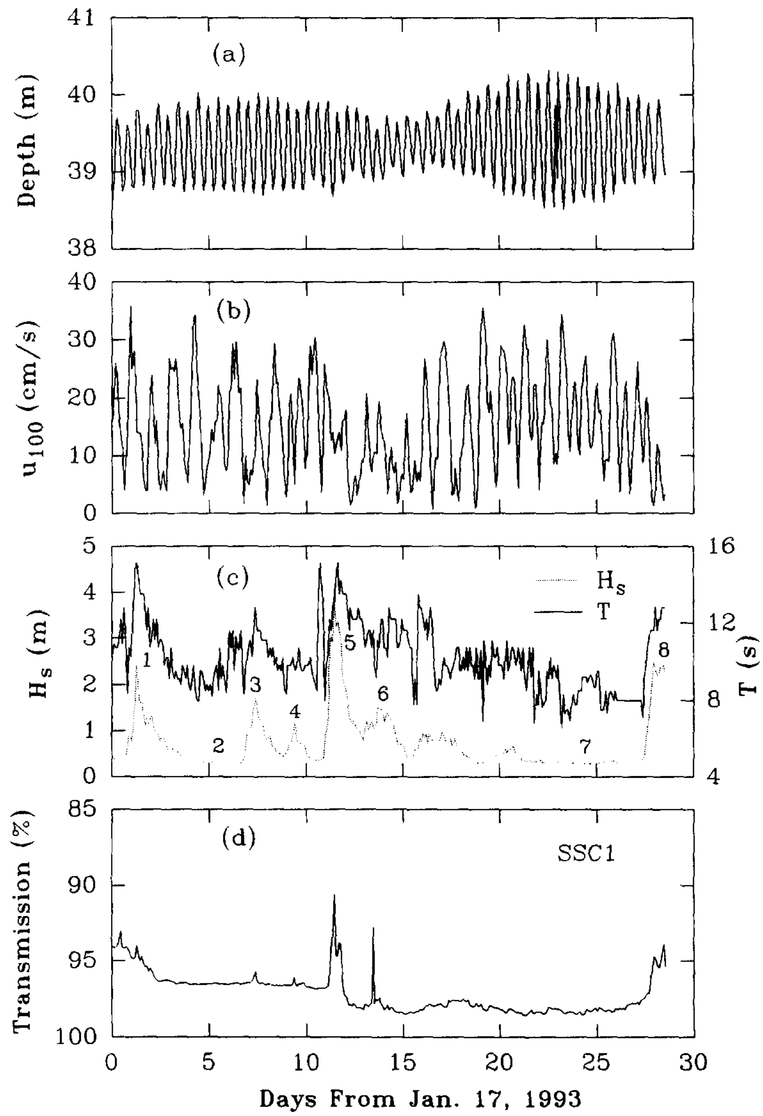

Fig. 2. Time series of the RALPH data collected during the 1992/93 winter deployment on Sable Island Bank: (a) mean water depth (m), (b) mean velocity 100 cm above the seabed (u_{100}, cm/s), (c) significant wave height (H_s, m) and peak spectral wave period (T, s), and (d) suspended sediment concentration (in transmission %).

suspended sediment concentration, SSC1, expressed in transmission percentage 0.7 m off the seabed for the entire experiment. The depth–time series in Fig. 2a clearly shows the semidiurnal tidal oscillation in the study region. One neap tide and two spring tides occurred during the experiment. The tide range was 0.5 m during the neap tide and increased to 1.5 m during the spring tide. The peak tidal current velocity was around 0.35 m/s during the spring tide, but reached only about 0.2 m/s during the neap tide (Fig. 2b). The dominant direction of the peak tidal flows was to the north, northeast and south, southwest.

Three significant storms occurred during the experiment and are marked as events 1, 5 and 8 in Fig. 2c, respectively. During these storms, significant wave heights were larger than 2 m and spectral peak wave periods were more than 13 s. Three lesser storms also occurred during the deployment (events 3, 4 and 6). H_s was between 1 to 2 m and T was around 10–12 s, respectively. Two calm periods occurred around days 6 and 25, during which H_s was smaller than 0.5 m and T was about 8 s. These are marked as periods 2 and 7 in Fig. 2c. Fig. 2a,b,c shows that storms did not affect surface elevation, but the tidal velocity oscillation was changed from semidiurnal for the non-storm condition (days 20–25) to nearly diurnal during storms (days 0–5 and days 10–15). The time series of the suspended sediment concentration in Fig. 2d shows three suspension events (at the beginning, the 12th day and the end of the deployment). These correspond with the three significant storms. Three minor peaks of SSC also occurred at day 7, day 9 and day 13 and were due to the passage of the three less-energetic storms (events 3, 4 and 6).

3.2. Sediment dynamics thresholds

Shields-type diagrams can be used to define bedload threshold for both unidirectional and oscillatory flows (Komar and Miller, 1975a; Madsen and Grant, 1975). Although Shields parameters have also been commonly used to determine bedload threshold under combined flows, data supporting their use under combined flows are very limited (Drake and Cacchione, 1986; Amos et al., 1988). The critical Shields parameter (θ_{cr}) is obtained in this study based on a modified Yalin (1977) method given in Miller et al. (1977). The Shields curve is divided into three segments:

$$\log\theta_{cr} = 0.045 \quad \sqrt{\Xi} > 3000 \tag{2a}$$

$$\log\theta_{cr} = 0.132\log\sqrt{\Xi} - 1.804 \quad 100 \leq \sqrt{\Xi} \leq 3000 \tag{2b}$$

$$\log\theta_{cr} = 0.041(\log\sqrt{\Xi})^2 - 0.356\log\sqrt{\Xi} - 0.977 \quad \sqrt{\Xi} < 100 \tag{2c}$$

where $\sqrt{\Xi}$ is the Yalin parameter defined as $[(\rho_s - \rho)gD^3/\rho v^2]^{0.5}$, in which ρ_s is the sediment density, ρ is the fluid density, g is the gravity acceleration and v is the kinematic fluid viscosity. For $D = 0.034$ cm at the study site, Eqs. (2a), (2b) and (2c) give $\theta_{cr} = 0.043$ and this means the critical shear stress $\tau_{cr} = \theta_{cr}(\rho_s - \rho)gD = 2.33$ dynes/cm^2 or a critical shear velocity $u_{*cr} = (\tau_{cr}/\rho)^{0.5} = 1.51$ cm/s.

Suspension according to Bagnold (1956) will occur when the vertical components of the turbulent velocity are roughly equal to the grain's settling velocity, w_s:

$$u_{*crs} = 0.8w_s \tag{3}$$

For $D = 0.034$ cm, the settling velocity w_s is 4.36 cm/s based on Gibbs et al. (1971). Thus the critical shear velocity for suspension u_{*crs} is equal to 3.49 cm/s from Eq. (3) and the critical Shields parameter for saltation/suspension will be $\theta_{crs} = 0.23$. As bed shear stress is further increased, ripples will be washed out and sediment transport occurs under the upper-plane bed sheet-flow condition. For unidirectional flows, Bagnold (1956) related the sheet flow critical Shields parameter (θ_{up}, 'up' in the subscript stands for upper-plane bed) with the sediment internal friction angle α and the bottom sediment volume concentration c_b: $\theta_{up} = c_b\tan\alpha$. For waves, Nielsen (1981) proposes that θ_{up} should be approximately 1.0 regardless of grain size. While the values of sediment internal friction angle itself is controversial and hard to determine (Miller and Byrne, 1966; Li and Komar, 1986), it is also intuitive that θ_{up} should be dependent on grain size. In contrast, Komar and Miller (1975b) use the wave-flume data of

Manohar (1955) to obtain the following θ_{up} function:

$$\theta_{up} = 0.413D^{-0.396} \tag{4}$$

where sediment grain size D must be in mm. The present study adopts this method because it is simple to use, dependent on grain size and is supported by laboratory data. When $D = 0.34$ mm is brought into Eq. (4), one obtains $\theta_{up} = 0.64$ or $u_{*up} = 5.8$ cm/s.

The time series of the combined wave–current shear velocity (u_{*cws}) predicted by the GM86 model is plotted in Fig. 3a in order to evaluate the critical shear stresses for various sediment transport phases under combined flows. Circles represent observed conditions of no transport, triangles are active rippled bed (bedload transport), squares indicate saltation/suspension and diamonds represent sheet flow conditions. The dashed lines define the established critical shear velocities for the initiation of bedload transport and for saltation/suspension as given by Eqs. (2a), (2b), (2c) and (3). When ripples were transitional (between wave and current forms), the complex ripple pattern prohibited any clear determination of ripple migration. Also when waves were pre-

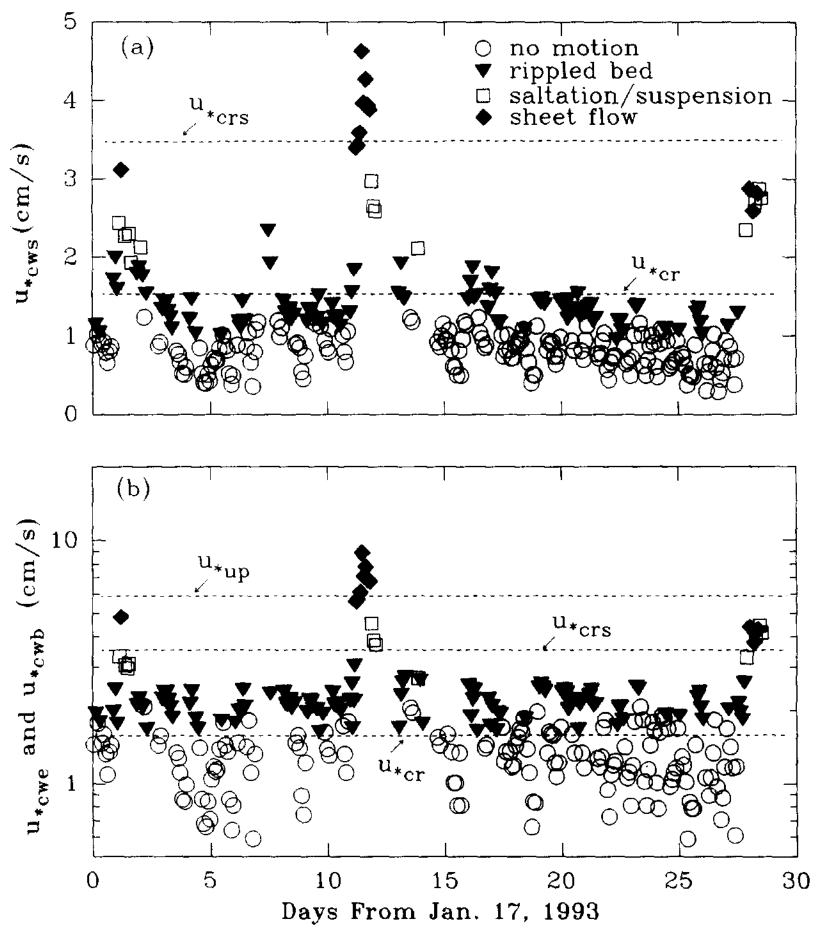

Fig. 3. Time series of the combined shear velocity: (a) the skin-friction shear velocity u_{*cws} predicted by the GM86 model using grain roughness only, and (b) the ripple-enhanced shear velocity u_{*cwe} (for bursts of $u_{*cws} < u_{*cr}$) and bedload shear velocity u_{*cwb} (for bursts of $u_{*cws} \geq u_{*cr}$). The bedload shear velocity was predicted using the sum of the grain roughness and the bedload roughness of Grant and Madsen (1982). The dashed lines represent the established critical shear velocities for bedload ($u_{*cr} = 1.51$ cm/s), saltation/suspension ($u_{*crs} = 3.49$ cm/s) and sheet flow ($u_{*up} = 5.8$ cm/s) transports, respectively.

dominant over currents, measured ripple migration rates were below the digitization resolution of GRASS. Thus observations of these conditions were not used in obtaining Fig. 3. No motion and bedload transport data are well separated in Fig. 3a, but the boundary between them is clearly below the established bedload critical shear velocity $u_{*cr} = 1.51$ cm/s. Also the separation between bedload and saltation/suspension at $u_{*cws} = 2$ cm/s as defined by the triangles and squares in Fig. 3a is significantly less than the established saltation/suspension threshold of $u_{*crs} = 3.49$ cm/s. The ripple wash out and sheet flow occurs around 3 cm/s as defined by the squares and diamonds. This value is again much below the critical value of $u_{*up} = 5.8$ cm/s given by Komar and Miller (1975b).

The poor agreement between the data for bedload motion and the established value $u_{*cr} = 1.51$ cm/s, however, does not necessarily mean that the GM86 model is under-predicting or that the Shields parameter is not applicable under combined-flow conditions. Seabed photos show that except during upper-plane bed bursts, the seabed was always covered by ripples. The Shields curve, however, is largely based on flat bed flume data. It is well established that when ripples are present, shear stress will increase from the ripple trough to the crest (Paola, 1983; Wiberg and Nelson, 1992; Li, 1994). Flume experiments by Kapdasli and Dyer (1986) and Kapdasli (1990) also demonstrate that the Shields curve can be used to determine the threshold shear stress over ripples under both unidirectional and combined wave–current flows as long as the maximum skin friction at the ripple crest is used. The GM86 model predicts the combined shear stress for an assumed flat bed and thus gives the spatially averaged shear stress, not the maximum at the ripple crest. Based on velocity measurements of Du Toit and Sleath (1981), Nielsen (1986) suggests the following method to obtain the ripple-enhanced shear velocity u_{*cwe} at the ripple crest:

$$u_{*cwe} = u_{*cws}/(1 - \pi\eta/\lambda) \tag{5}$$

Wiberg and Nelson (1992) obtained a similar function based on their shear stress measurements over symmetric ripples. Due to the lack of a tested ripple predictor for combined flows, the average ripple steepness $\eta/\lambda = 0.125$ for the site-1 data was used in Eq. (5) to calculate u_{*cwe} and these ripple-enhanced shear velocities are plotted in Fig. 3b for the no-motion bursts and those bedload bursts in which $u_{*cws} < u_{*cr}$. A clear separation between the no-motion (circles) and rippled-bed (triangles) data is again defined and this separation is in excellent agreement with the critical shear velocity $u_{*cr} = 1.51$ cm/s as given by the standard Shields curve. This agreement thus suggests that the standard Shields parameter is applicable to the combined-flow conditions, but it has to be compared to the *enhanced combined* shear velocity at the ripple crest when ripples are present. If the calculation of u_{*cwe} in Eq. (5) is correct, it provides indirect evidence that the Grant and Madsen combined-flow bbl model gives adequate predictions of the combined skin-friction shear velocity inside the wave boundary layer.

The large discrepancy between the data defined saltation/suspension and sheet flow thresholds and the established values according to Bagnold (1956) and Komar and Miller (1975b) seen in Fig. 3a is more difficult to explain. We believe that the enhanced shear velocity at the ripple crest, u_{*cwe}, can only cause very localized saltation/suspension and it is the average shear velocity that causes the observed overall suspension transport. In high transport stages, ripple height is also dramatically reduced making the enhancement of shear velocity at the ripple crest insignificant. For these reasons, the average shear velocity has to be used in defining suspension and sheet flow criteria. Wave motion has been parameterized quite differently by various investigators using the significant wave height, H_s (Huntley and Hazen, 1988; Amos et al., 1988; Green et al., 1990), one-tenth largest waves, $H_{1/10}$ (Larsen et al., 1981; Drake and Cacchione, 1986) and the maximum wave height, H_m (Grant et al., 1984). $H_{1/10}$ has also been used in the GM86 model for this study and this causes a 15–20% increase in u_{*cws} which is still much below the standard threshold values. The GM86 model uses only grain size roughness height $k_{bg} = 2.5D$ to predict skin-friction shear velocity, even under the suspension and sheet flow conditions. When sediment transport occurs, however, a portion of the flow power is spent in overcoming the grain-to-grain friction force and maintaining a thin bedload transport layer. Based on analytical analyses and pressure-conduit data, Wilson (1988) showed that the friction factor at high transport stages was poorly controlled by the grain size roughness, but it correlated well with the thickness of the bedload layer. In partitioning skin friction from form drag over bedforms (Smith and McLean, 1977; Wiberg and Nelson, 1992; Li, 1994) and in calculating sediment transport rates for steady flows (Nielsen, 1992), the sum of the grain roughness height k_{bg} and the roughness height due to bedload transport, k_{bt}, has generally been used to obtain a transport-related shear stress. In light of these considerations, the original bedload roughness height algorithm of Grant and Madsen (1982) was used to calculate the thickness scale of the bedload layer, h_{tm}, and the bedload roughness height k_{bt}:

$$h_{tm} = 42(\rho_s/\rho + 0.5)D\theta_{cr}[(\theta_{cws}/\theta_{cr})^{0.5} - 0.7]^2 \quad (6a)$$

$$k_{bt} = 3.8h_{tm} \quad (6b)$$

where $\theta_{cws} = \rho u_{*cws}^2/(\rho_s - \rho)gD$ is the skin-friction combined Shields parameter. The sum of k_{bg} and k_{bt} from Eqs. (6a) and (6b) was then used in the GM86 model to compute the bedload shear velocity u_{*cwb}. The values of u_{*cwb} predicted in this way are re-plotted in Fig. 3b for the suspension/sheet-flow bursts and those bedload bursts where $u_{*cws} \geq u_{*cr}$. For those bedload bursts of $u_{*cws} < u_{*cr}$, only weak sediment transport occurs at the ripple crest (due to $u_{*cwe} > u_{*cr}$) and bedload roughness is probably less significant. Thus u_{*cwb} was not computed for these bursts. At moderate transport stages, we find the transition from bedload transport (triangles) to saltation/suspension (squares) to be well separated. But the value of u_{*cwb} at this transition is only around 2.8 cm/s and significantly less than the theoretical $u_{*crs} = 3.49$ cm/s. At higher transport stages, the predicted bedload shear velocity at the transition from suspension to sheet flow is at about 4.5 cm/s and this is much below the sheet flow criterion of 5.8 cm/s. However, wave tunnel measurements by Sawamoto and Yamashita (1986) show that the bedload layer height ranges from 2 to 6 times the grain diameter under sheet flow conditions. Eq. (6a) predicts h_{tm} to be $60D$ at the sheet flow threshold $u_{*up} = 5.8$ cm/s, about one order of magnitude too high. Therefore it seems that the bedload roughness algorithm of Grant and Madsen (1982) over-predicts the thickness scale of the bedload layer, but under-predicts the bedload roughness height k_{bt} due to the small proportionality coefficient in Eq. (6b). We thus conclude that the bedload roughness method of Grant and Madsen (1982) does not apply under the combined-flow conditions.

Based on the steady-flow flume data of Guy et al. (1966) and a function proposed by Dietrich (1982), Wiberg and Rubin (1989) suggest the following:

$$h_{tm} = 0.68D\tau_*/(1 + a_2\tau_*) \quad (7)$$

where $\tau_* = \tau_{cws}/\tau_{cr}$ is the normalized shear stress and a_2 is a grain size related coefficient given by $a_2 = 0.0204(\ln D)^2 + 0.022\ln D + 0.0709$. Bedload roughness height is then related to h_{tm} through:

$$k_{bt} = 1.68h_{tm} \quad (8)$$

This bedload roughness height was used to run the GM86 model and the predicted bedload shear velocity is plotted in Fig. 4a in a similar fashion as in Fig. 3b. In comparison with the established criterion of u_{*crs} and u_{*up}, the Wiberg and Rubin method clearly under-predicts the bedload shear stress under the combined flows: the values of u_{*cwb} at the transition from bedload to suspension and that from suspension to sheet flow are only about 2.5 and 3.3 cm/s, respectively. Based on the laboratory measurements of energy dissipation rate under oscillatory flows of Carstens et al. (1969) and the unidirectional flume data of Wilson (1966) on bedload transport under high shear stresses, Nielsen (1992) suggests that bedload roughness height under waves is about one order of magnitude higher than under unidirectional flows for a given shear stress. Since Wiberg and Rubin based their function on the unidirectional flume data of Guy et al. (1966), it will under-predict bedload roughness height and hence the bedload shear velocity for suspension and sheet-flow transport modes.

Based on the wave tunnel measurements of Sawamoto and Yamashita (1986) and the theoreti-

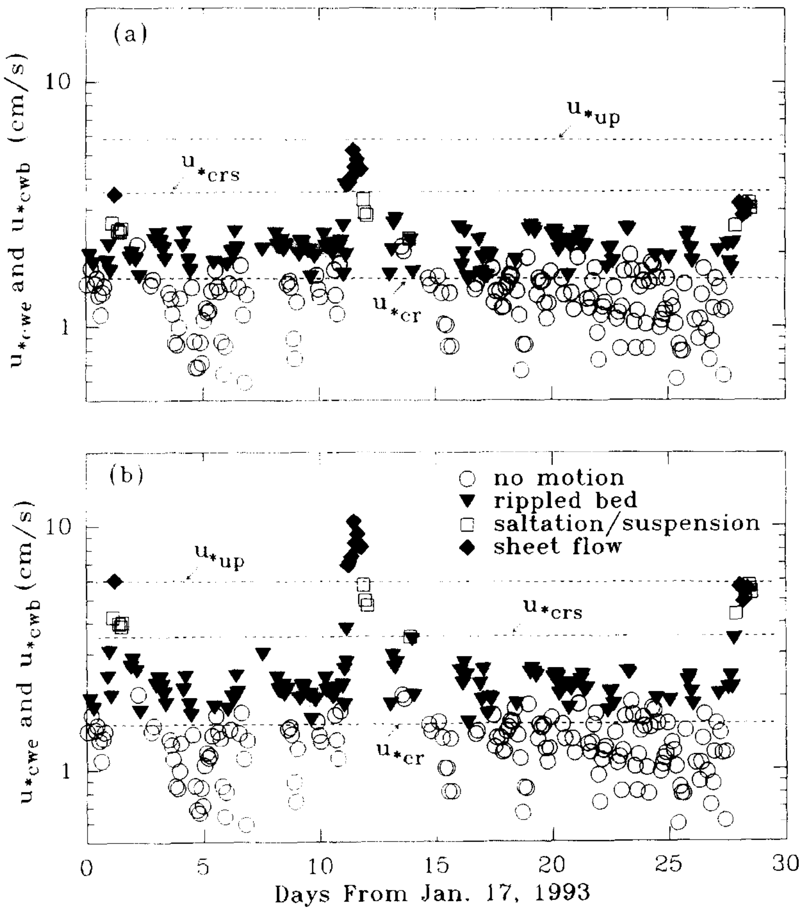

Fig. 4. Time series of the ripple-enhanced shear velocity u_{*cwe} (for bursts of $u_{*cws} < u_{*cr}$) and bedload shear velocity u_{*cwb} (for bursts of $u_{*cws} \geq u_{*cr}$). The bedload roughness is calculated according to Wiberg and Rubin (1989) in (a) and a modified method based on Nielsen (1992) in (b). The dashed lines are as defined in Fig. 3.

cal arguments of Nielsen (1992), we propose the following algorithm for the prediction of bedload layer height for combined waves and currents:

$$h_{tm} = 2.9D(\theta_{cws} - \theta_{cr})^{0.75} \tag{9}$$

This function was used to compute h_{tm} and Eq. (6b) with an adjusted proportionality coefficient was used to calculate the bedload roughness height k_{bt}. The sum of this k_{bt} and the grain roughness height was then used in the GM86 model to compute the bedload shear velocity u_{*cwb}. The proportionality in Eq. (6b) was adjusted so that the model-predicted u_{*cwb} at the transition from suspension to sheet flow was approximately equal to the established sheet-flow threshold $u_{*up} = 5.8$ cm/s. This adjusting gave us

$$k_{bt} = 180h_{tm} \tag{10}$$

The bedload shear velocities calculated from the GM86 model using Eqs. (9) and (10) are plotted in Fig. 4b for the suspension/sheet-flow bursts and those bedload bursts in which $u_{*cws} \geq u_{*cb}$. The predicted u_{*cwb} at the transition from suspension to sheet flow now agrees well with the established $u_{*up} = 5.8$ cm/s as it should due to the proportionality adjustment in Eq. (10). However, the value of u_{*cwb} at the transition from bedload to suspension is also in good agreement with the suspension threshold $u_{*crs} = 3.49$ cm/s. This lends support to our adjustment in Eq. (10) and suggests that bedload shear velocity due to the sum of grain and bedload roughnesses should be compared against the established threshold shear velocities to properly determine the onsets of suspension and sheet-flow transport modes under combined-flow conditions.

3.3. Wave–current interaction

Data from several field experiments have shown that the GM model adequately predicts the enhanced total current shear velocity (u_{*c}) and apparent roughness (z_{0c}) above the wave boundary layer and that the enhancement is due to the wave–current interaction under the combined flows (Grant et al., 1984; Cacchione et al., 1987; Huntley and Hazen, 1988; Green et al., 1990; Drake and Cacchione, 1992). Since velocity was only measured at two heights in this study, we can not derive reliable u_{*c} and z_{0c} from the velocity data to test the GM86 model. In this section, bed stress estimates from the GM86 model are compared to calculations using the quadratic stress law to quantify the enhancements of shear stress and bed roughness over a medium sand bed under a large range of wave and current strengths.

For steady currents, the bed shear stress can be obtained from the quadratic drag law:

$$\tau_c = \rho C_{100} u_{100}^2 \tag{11}$$

where C_{100} is the drag coefficient at 100 cm above the bed. Total current shear velocity is then computed from $u_{*c} = (\tau_c/\rho)^{0.5}$. The typical value of C_{100} over a rippled sand bed (as is the case here) is 0.003 (Sternberg, 1972). This C_{100} value and measured u_{100} were used in Eq. (11) to obtain the drag-coefficient-based total current shear velocity, u_{*c-CD}, for each burst. Assuming no wave effect, this u_{*c-CD} should be due to the total roughness:

$$z_{0c-GR} = 2.5D/30 + 27.7(\eta^2/\lambda)/30 \tag{12}$$

where the ripple roughness height $27.7(\eta^2/\lambda)$ is based on Grant and Madsen (1982); η and λ are predicted by a combined-flow ripple predictor (Li and Amos, 1997) based on the data from Sable Island Bank. In order to quantify the enhancement of u_{*c} and z_{0c} due to wave–current interaction only, the GM86 model was run using grain and ripple roughnesses with bedload roughness being eliminated. In this case, the model-predicted total current shear velocity, u_{*c-M}, and the apparent bottom roughness, z_{0c-M}, were only due to the grain-ripple roughness plus the wave–current interaction. The ratio of u_{*c-M}/u_{*c-CD} is plotted as a time series in Fig. 5a, while the time series of z_{0c-GR} and z_{0c-M} are compared in Fig. 5b. Figs. 5c and 5d, respectively, show the time series of C_{100} based on the model-predicted total current shear velocity and the ratios of u_b/u_{100}; u_b here is the near-bed wave orbital velocity. Fig. 5a shows that the total current shear velocity was enhanced by 20% during non-storm periods (marked 2 and 7 in

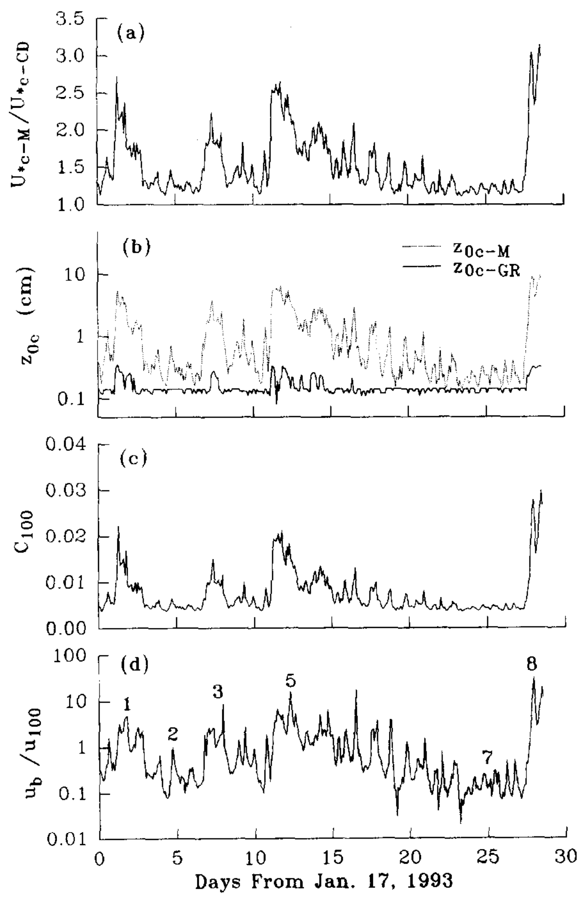

Fig. 5. (a) The ratio of u_{*c-M}/u_{*c-CD}, (b) z_{0c-GR} and z_{0c-M}, (c) C_{100}, and (d) the ratio of u_b/u_{100} plotted as a function of time to quantify the enhancement of total current shear velocity and apparent bottom roughness due to wave–current interaction. See text for definition and explanation.

Fig. 5d), while the wave-enhanced u_{*c} reached 2–3 times higher than the drag-coefficient-based u_{*c-CD} during storms (1, 3, 5 and 8 in Fig. 5d). The comparison of z_{0c-M} and z_{0c-GR} in Fig. 5b indicates that the apparent roughness felt by the steady current above the wave boundary layer was increased more than one order of magnitude during storms, the maximum values reaching about 10 cm. This roughness enhancement was 2–3 times even during the current-dominated non-storm periods. The average C_{100} based on model-predicted u_{*c} was 0.0074, about 2.5 times the conventional value of 0.003 for rippled beds. It is also interesting to note that the model-predicted C_{100} ranged from 0.021 to 0.027 during storms, but decreased to 0.004 (close to the conventional C_{100} value) on the average during the non-storm periods ($u_b/u_{100} < 1$).

It has been well accepted that wave and current motions cannot be treated separately and then superposed to get the combined shear stress, but rather non-linear coupling of the two has to be considered. Past studies have concentrated on the enhanced total current shear velocity and apparent bed roughness above the wave boundary layer, but few have quantitatively evaluated the enhancement of the skin-friction shear velocity inside the wave boundary layer. In order to do so, we use the simple method of Swart (1974) to calculate pure wave friction factor:

$$f_w = \exp[5.213(k_{bg}/A_b)^{0.194} - 5.977] \tag{13}$$

where $k_{bg} = 2.5D/30$ is again the grain roughness height and A_b is the near-bed wave orbital amplitude. The skin-friction wave shear stress (hence wave shear velocity u_{*ws}) is then obtained from $\tau_{ws} = 0.5\rho f_w u_b^2$. The conventional $C_{100} = 0.0015$ of Sternberg (1972) for smooth sand bottom is used in Eq. (11) to calculate the skin-friction current shear velocity and stress (τ_{cs}). τ_{ws}, τ_{cs} and the angle between the wave and current (ϕ_b) are then used to vectorially compute the linearly added skin-friction combined shear velocity u_{*cws-L}. The ratio of the model-predicted u_{*cws} to u_{*cws-L} is plotted as a time series in Fig. 6 (the upper curve) in comparison with the time series of u_{*ws}/u_{*cs} (the lower curve). Fig. 6 shows that the non-linear coupling has increased the skin-friction shear velocity by as much as 20% compared to the linear-addition calculation. When either waves or currents are dominant ($u_{*ws}/u_{*cs} \gg 1$ or $\ll 1$), non-linear coupling is weak and the enhancement of u_{*cws} is generally less than 5%. Troughs T1, T3 and T5 in Fig. 6 correspond to wave-dominated condition, while troughs T2 and T4 are current-dominated cases. In contrast, the maximum enhancement of u_{*cws} due to non-linear coupling generally occurs when waves and currents are of equal strength ($u_{*ws}/u_{*cs} \approx 1$, see peaks P1, P3 and P5 in Fig. 6) or waves are slightly stronger than currents (u_{*ws}/u_{*cs} slightly higher than 1, peaks P2 and P4).

The angle between waves and current, ϕ_b, also affects the non-linear interaction and u_{*cws} enhancement. The ratio of the model-predicted to linearly added u_{*cws} is plotted in Fig. 7 as a function of ϕ_b for various relative strengths of waves vs. currents. The circles, triangles, squares and diamonds in the diagram represent u_{*ws}/u_{*cs} of 0.5, 1.0, 1.5 and 3.0, respectively. The individual data curve for each fixed u_{*ws}/u_{*cs} ratio as well as the combined data trend show that the enhancement of u_{*cws} due to non-linear coupling over the linear addition decreases from 20% to about 5% as the angle between waves and current is increased from $<20°$ to about 90°. This effect of relative wave–current direction appears to become negligible when ϕ_b is approximately less than 20°. For a fixed angle between waves and current, Fig. 7 shows that the maximum enhancement of u_{*cws} due to non-linear coupling is for $u_{*ws}/u_{*cs} = 1.0$ (the curve defined by triangles in Fig. 7) and this enhancement becomes weaker when u_{*ws}/u_{*cs} is either larger or smaller than 1.0. For instance, the maximum u_{*cws} ratio is about 1.2 for $u_{*ws}/u_{*cs} = 1.0$ data group at $\phi_b = 40°$. This ratio decreases to 1.15 for current-dominated conditions ($u_{*ws}/u_{*cs} = 0.5$) and drops further to 1.10 for the wave-dominated bursts ($u_{*ws}/u_{*cs} = 3.0$). This finding further supports the conclusion drawn from Fig. 6.

3.4. *Sediment transport predictions*

Many sediment transport formulae have been proposed for use under unidirectional flows and

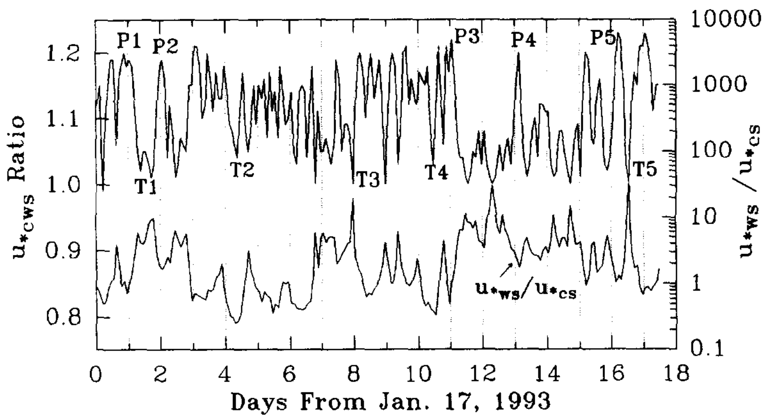

Fig. 6. Time series of the ratio of model-predicted skin-friction combined shear velocity, u_{*cws}, vs. the linearly added skin-friction combined shear velocity, u_{*cws-L}, in comparison with the relative wave–current strength, u_{*ws}/u_{*cs}.

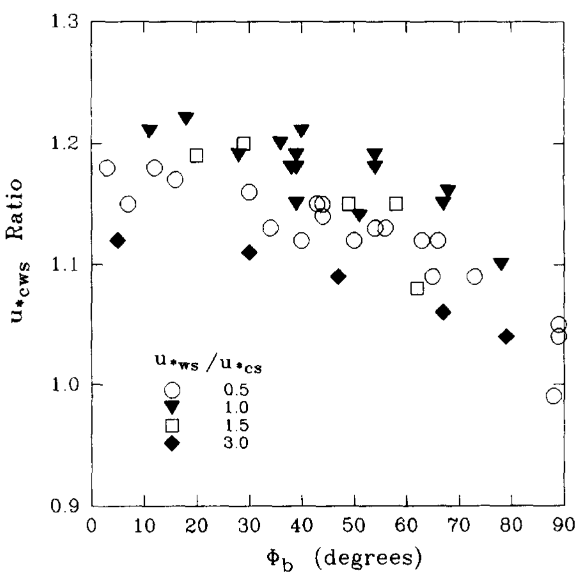

Fig. 7. The variation of model-predicted vs. linearly added skin-friction combined shear velocity, u_{*cws}/u_{*cws-L}, as a function of the angle between waves and current, ϕ_b. Circles, triangles, squares and diamonds represent $u_{*ws}/u_{*cs}=0.5$, 1.0, 1.5 and 3.0, respectively.

they have been extensively compared with river or flume data (Ackers and White, 1973; White et al., 1975). There have been few attempts to test the use of these formulae under combined waves and currents. Results of radioactive and fluorescent tracer experiments have been used by various investigators to evaluate the applicability of these unidirectional sediment transport formulae in the marine environment (Gadd et al., 1978; Heathershaw, 1981; Lees, 1983; Pattiaratchi and Collins, 1985). These studies show that the difference between the measured and predicted transport rates and among the predictions by various formulae can be more than one order of magnitude. There is no consensus on the best formula for prediction in the marine environment. Kachel and Sternberg (1971) measured velocity profiles and ripple migration rates in a tidal channel to compare various transport formulae. Based on the total shear velocity obtained from the velocity profiles, they found that a modified Bagnold bedload formula gave reasonable predictions. The only attempt that used measured ripple migration rates to test unidirectional transport formulae under combined waves and currents is that of Amos et al. (1997). Based on the ripple migration rates and tripod data collected on the Scotian Shelf in 1982, they find that when wave shear velocity of Grant and Madsen (1979) is combined with the current shear velocity based on a constant $C_{100}=0.003$, the Einstein–Brown (Brown, 1950) bedload formula gave reasonable prediction compared to the measured bedform transport rates. However, ripple height was not measured in the 1982 experiment and was calculated from a current ripple relationship according to Allen (1970). Ripple height, ripple migration rates and boundary layer dynamics were all measured under variable conditions in this study. Armed with more advanced combined-flow bbl theory, we intend to use these data to evaluate the applicability of various unidirectional-flow transport formulae under combined flows and to examine the sediment transport patterns under storm and non-storm conditions in this section.

The bedload sediment transport rate can be obtained by considering the volume of sediment involved in the migration of ripples. For ripples of height η and migration rate R_m, the mean mass transport rate per unit width per unit time will be:

$$q_m = 0.5\rho_b \eta R_m \tag{14}$$

where ρ_b is the bulk sediment density (=1.8 g/cm^3). Kachel and Sternberg (1971) suggested that the maximum transport rate at the ripple crest should be twice that given by Eq. (14). We are, however, more concerned with the mean transport rate.

A continental shelf sediment transport model (SEDTRANS) has been developed at the Geological Survey of Canada (Atlantic) (Martec Ltd., 1984, 1987; Davidson and Amos, 1985; Amos and Judge, 1991). This model has recently been upgraded to SEDTRANS92 by Li and Amos (1995). SEDTRANS92 incorporates the following unidirectional sediment transport formulae.

The Engelund and Hansen (1967) total-load equation:

$$q_s = 0.05Du_{100}^2\rho^2 u_*^3/[D(\Delta\rho g)^2] \tag{15}$$

where q_s is the volume rate of sediment transport, u_* is the skin-friction shear velocity and $\Delta\rho$ is equal to $\rho_s - \rho$;

The Einstein–Brown (Brown, 1950) bedload equation:

$$q_s = 40Dw_s(\rho/\Delta\rho gD)^3 u_*^5 |u_*| \tag{16}$$

where w_s is the sediment grain settling velocity given by Gibbs et al. (1971);

The Bagnold (1963) total-load equation:

$$q_s = K\rho u_{*cws}^2 u_{100}/(\rho_s - \rho)g \tag{17a}$$

$$K = 0.005\exp(0.7S) \tag{17b}$$

where K is the proportionality coefficient according to Sternberg (1972) and $S = \tau_{cws}/\tau_{cr} - 1$ is the normalized excess shear stress; and

The Yalin (1963) bedload equation:

$$q_s = 0.635Du_*[S - (1/a)\ln(1 + aS)] \tag{18}$$

where the empirical coefficient a is equal to $2.45(\rho/\rho_s)^{0.4}(\tau_{cr}/\Delta\rho gD)^{0.5}$. The instantaneous combined skin-friction shear velocity u_{*cws} is compared to the critical shear velocity u_{*cr} to determine if sediment transport will occur. The x and y components of sediment transport are considered separately, where x is parallel to the wave direction and y is normal to the wave direction. The current and wave shear velocities and the angle between them given by the GM86 model are used to vectorially compute the shear velocities and hence sediment transport rates in the x and y directions, respectively. The x and y components of the instantaneous sediment transport rate so calculated are integrated over a wave cycle and divided by the wave period to determine the average sediment transport rates in these directions. These average transport rates are then added vectorially to obtain the time-averaged total sediment transport rate and direction. The Bagnold method assumes that waves cause sediment entrainment, while currents cause net transport. Thus integration is not required. The details of model structure, theories and operation are given in Li and Amos (1995).

The measured sediment transport rates are compared with the predicted transport rates by the Engelund–Hansen method in Fig. 8a and Fig. 8b. The average combined skin-friction shear velocity, u_{*cws}, of the GM86 model was used to determine the threshold for bedload transport in Fig. 8b. The plots show that though the predicted transport magnitude is comparable to that of the bedform transport rates, SEDTRANS92 significantly under-predicts sediment transport frequency and duration. The model predicts no transport for many bursts, yet ripple migration was clearly measured. This under-prediction is most likely due to the use of the average shear velocity over a rippled bed (as discussed in Section 3.2). Based on the measured ripple geometry, the ripple-enhanced combined shear velocity, u_{*cwe}, as given by Eq. (5), was used to determine the threshold of bedload transport in running SEDTRANS92 (but the average skin-friction shear velocity u_{*cws} was still

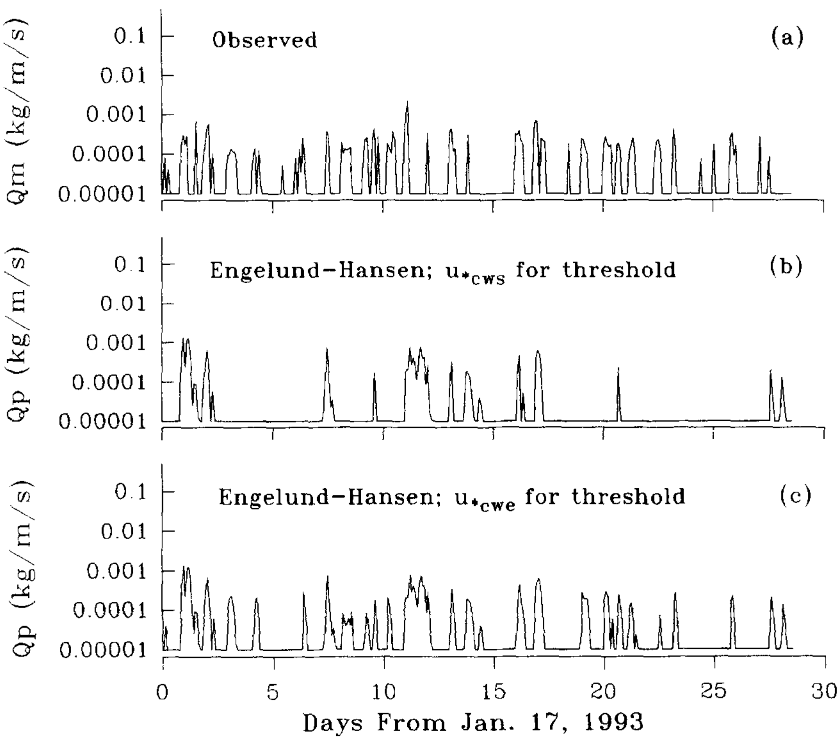

Fig. 8. Time series of (a) measured bedload sediment transport rate, Q_m, in comparison with the predicted sediment transport rates, Q_p, by the Engelund–Hansen formula using (b) the skin-friction shear velocity, u_{*cws} and (c) the ripple-enhanced shear velocity, u_{*cwe}, for bedload threshold determination.

used in the calculation of sediment transport rates) and the result is shown in Fig. 8c. Comparing Figs. 8a and 8c indicates that the use of this ripple-enhanced shear velocity has increased the frequency of the predicted sediment transport events so that the model predictions are in better agreement with the measured bedform transport rates. Closer examination of (a) and (c) in Fig. 8, however, shows that the Engelund–Hansen total-load method still under-predicts for most of the transport peaks and, for some sediment transport bursts, the model still predicts zero transport (about 26% of the total transport bursts). This under-prediction is expected since the GM86 model assumes wave-dominated conditions, but currents were stronger than waves during a significant portion of the 1992 Sable Island Bank experiment. The Smith (1977) model is applicable under current-dominant combined flows, but it significantly under-estimates the wave shear stress under storm conditions and is not compatible with the GM86 model. Amos et al. (1988, 1997) have found that using the GM wave shear stress and a simple current shear stress based on $C_{100}=0.003$ of Soulsby (1983) best predicts the bedload transport rates under current-dominant combined flows. The same approach is adopted here to replace the GM current shear velocity with the current shear velocity based on $C_{100}=0.003$ in running SEDTRANS92 when currents are dominant over waves. The time series of the predicted sediment transport rates are plotted in Fig. 9 for all of the four formulae. Comparing the Engelund–Hansen predictions in Fig. 9a with Fig. 8, we find that the incorporation of the Soulsby current shear velocity in the model gives the best predictions of sediment transport magnitude and frequency. A careful comparison between Figs. 9 and 8a also indicates the following. (a) Though the Engelund–Hansen total-load method correctly predicts the magnitude of sediment transport rates under low to moderate energy levels, it fails to predict any increase in

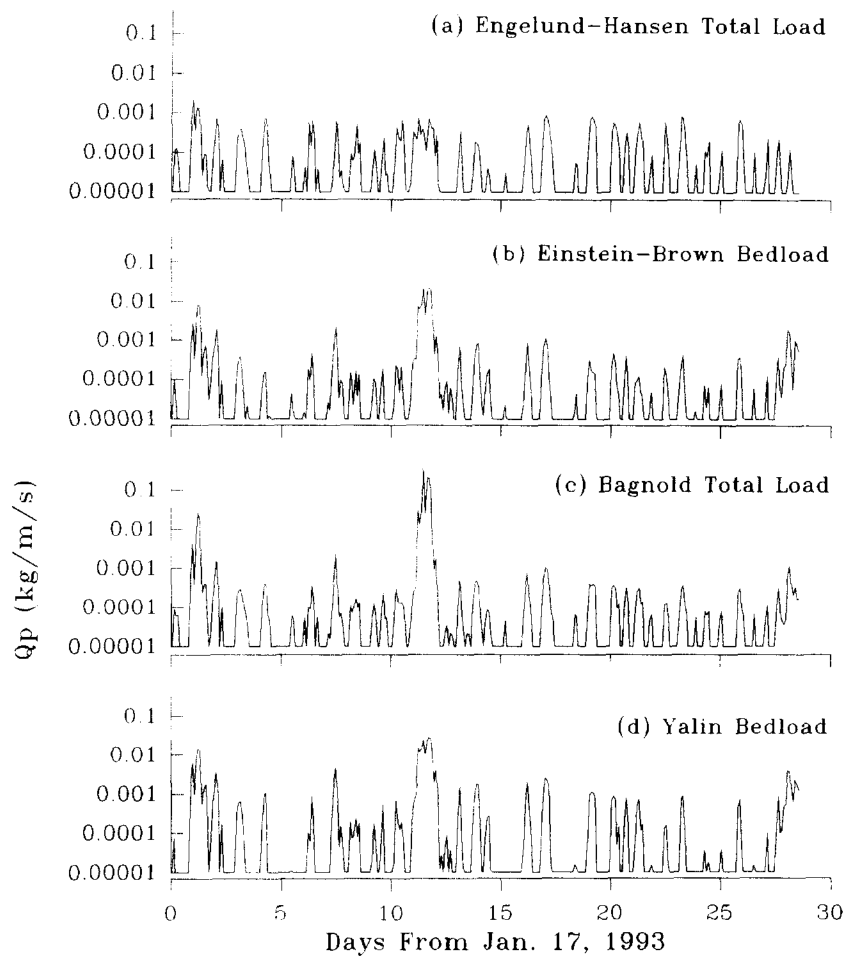

Fig. 9. Time series of model-predicted sediment transport rates based on (a) the Engelund–Hansen total-load formula, (b) the Einstein–Brown bedload formula, (c) the Bagnold total-load formula, and (d) the Yalin bedload formula.

sediment transport rate during the storms at days 2, 12 and 28, respectively. Thus it cannot be used for total load prediction under storm conditions on continental shelves. (b) The transport frequency is under-predicted by the Yalin bedload method, yet the overall magnitudes are over-predicted. (c) Both sediment transport magnitude and frequency under low to moderate energy are correctly predicted by the Einstein–Brown bedload method and the Bagnold total-load method. These formulae also predict significant increases in sediment transport rates during the storms and thus seem to be most promising for application to combined flows on continental shelves.

The scattergrams of measured and predicted sediment transport rates are given in Fig. 10 for the various formulae in order to further examine the applicability of these methods to the combined waves and currents on the continental shelf. The dashed lines represent the perfect agreement and the triangles are the data for fine sand collected during a similar field experiment conducted on the Sable Island Bank in 1982. The data in Fig. 10 only include those bursts for which the bedload shear velocity, u_{*cwb}, is below the ripple breakoff threshold of Grant and Madsen (1982) so that contamination of transport rates due to sand saltation, bypassing, and suspension is avoided. These plots show that the Yalin method (Fig. 10d) under-predicts for low transport rates, but over-predicts

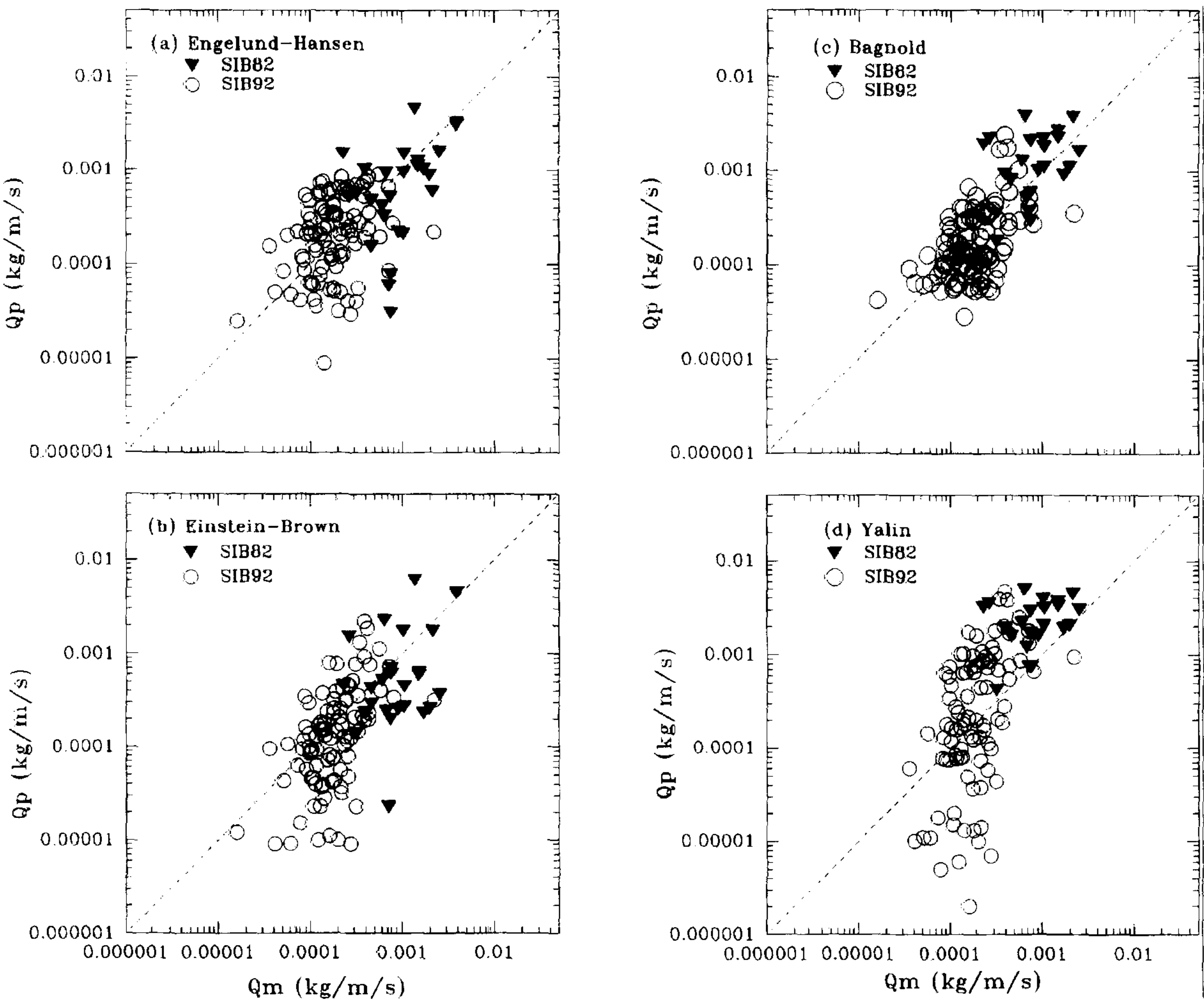

Fig. 10. Scatter plots of the measured vs. predicted sediment transport rates for (a) the Engelund–Hansen total-load formula, (b) the Einstein–Brown bedload formula, (c) the Bagnold total-load formula, and (d) the Yalin bedload formula. Circles represent data from the present study over medium sand, and triangles are the 1982 Sable Island Bank data over fine sand.

for high transport bursts. While the Engelund–Hansen, Einstein–Brown and Bagnold methods all seem to give reasonable prediction with an error less than one order of magnitude, the Bagnold method produces the least scatter (Fig. 10c). The Engelund–Hansen, Einstein–Brown and Bagnold methods are further compared as time series in Fig. 11 for the bursts in which bedload sediment transport rate has been measured. A similar comparison is also shown in Fig. 12 for the 1982 Sable Island Bank data over fine sand sediment ($D = 0.23$ mm). All three formulae again show good predictions compared to the measured bedform transport rates. However, suspended load transport should become dominant for fine sand deposits during storms and thus a total-load formula should predict higher transport rates than a bedload formula under such conditions. For the medium sand of the 1992 data, suspended load transport seldom occurred. Both the Bagnold and Engelund–Hansen total-load formulae give roughly the same predictions of sediment transport rates as that of the Einstein–Brown bedload method (Fig. 11a,b). For the fine sand of

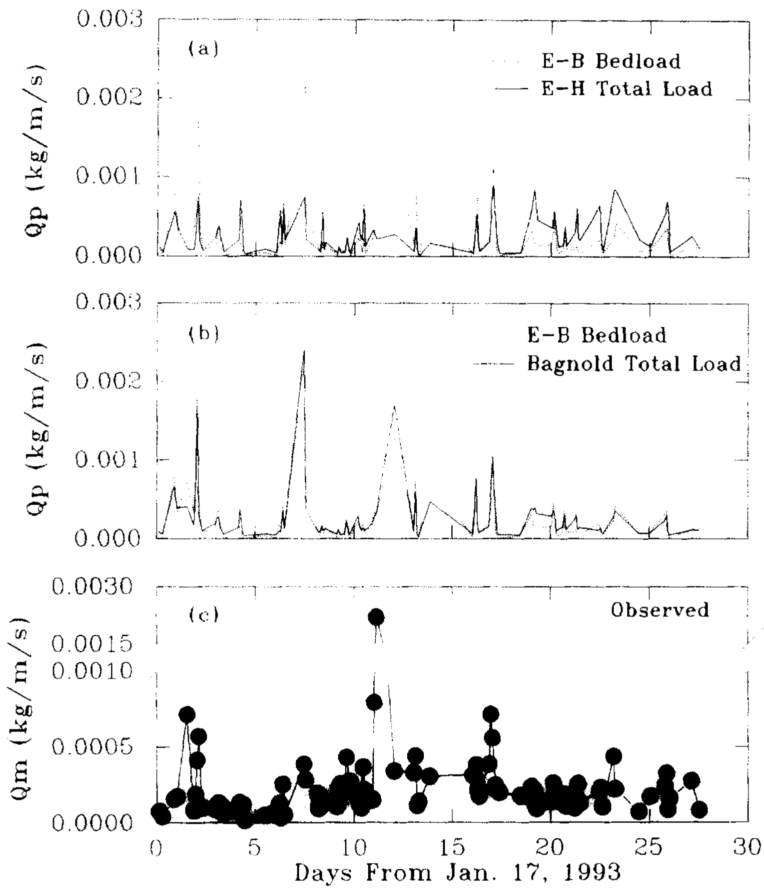

Fig. 11. Time series of the predicted sediment transport rates using (a) the Engelund–Hansen total-load and Einstein–Brown bedload formulae, and (b) Bagnold total-load formula in comparison with (c) the measured bedform transport rates for the present study.

the 1982 data, the Bagnold formula correctly predicts significantly higher sediment transport rates compared to the predictions of the Einstein–Brown bedload method under the storm around day 15 in Fig. 12, while the Engelund–Hansen formula fails to do so. We conclude that while the Engelund–Hansen, Einstein–Brown and Bagnold methods all give reasonable predictions of the bedload transport rate under combined waves and currents, the Bagnold total-load method should be used to predict the total sediment transport rates under the storm conditions. The Yalin method does not give adequate predictions of sediment transport under the present observational conditions.

The capability to predict sediment transport direction under combined flows is no better than that for transport rate. Pattiaratchi and Collins (1984) found that predicted bedload transport direction under combined waves and currents was eastward in the Bristol Channel which was opposite to the transport direction suggested by sand wave/megaripple orientations. Based on the discrepancy between model-predicted and tracer-derived sediment transport directions for the Venture discovery site on Sable Island Bank, Hodgins and Sayao (1986) also raised doubt about the assumption that waves only stir up sand and currents determine net sediment transport. Amos et al. (1997) have compared ripple patterns and directions of waves and currents under low-energy summer conditions on the Scotian Shelf. They propose that wave- and current-formed ripples co-exist under combined flows and current ripples

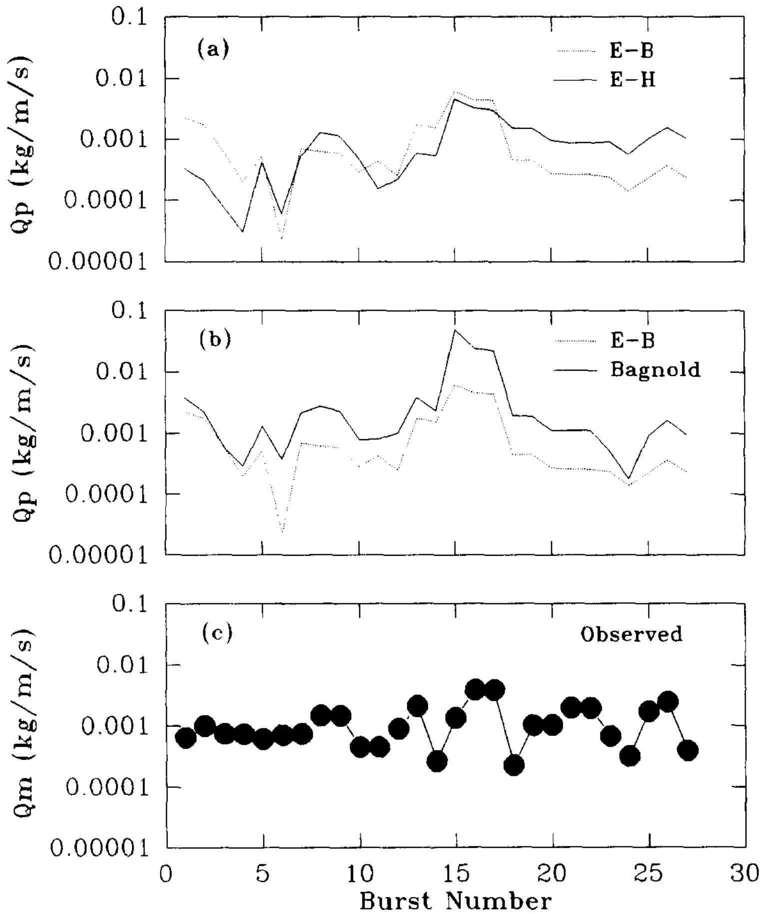

Fig. 12. Time series of the predicted sediment transport rates using (a) the Engelund–Hansen total-load and Einstein–Brown bedload formulae, and (b) Bagnold total-load formula in comparison with (c) the measured bedform transport rates for the 1982 Sable Island Bank data over fine sand sediment.

generally migrate in the current direction for current-dominant combined flows. Under combined waves and currents, although waves oscillate $\pm 180°$, the residual combined shear stress is in the direction for which the wave stress forms an acute angle with the co-existing current stress. Thus the net sediment transport should be between the wave and current directions, following the direction of the combined shear stress, τ_{cws} (see details in Li and Amos, 1995). The measured ripple migration direction of the present study is plotted in Fig. 13 against the model-predicted sediment transport direction using the Bagnold total-load method. If ripple migration and predicted transport directions are, respectively, in the NW and NE quadrants, 360° is then added to the smaller value to be used in obtaining Fig. 13. Fig. 13 clearly shows that the model-predicted transport directions agree reasonably well with the measured ripple migration directions, the predicted directions being 30° higher than the ripple migration direction on average.

Assuming that the Bagnold total-load formula gives adequate prediction of the total sediment transport rate and direction under combined flows, the time series of the net daily sediment transport rate (kg m^{-1} day^{-1}) and direction (true north) are plotted in Fig. 14 in comparison with the skin-friction wave shear velocity, u_{*ws}. The net daily transport rates during storms (days 2 and 12) were 2 to 3 orders of magnitude higher than that during

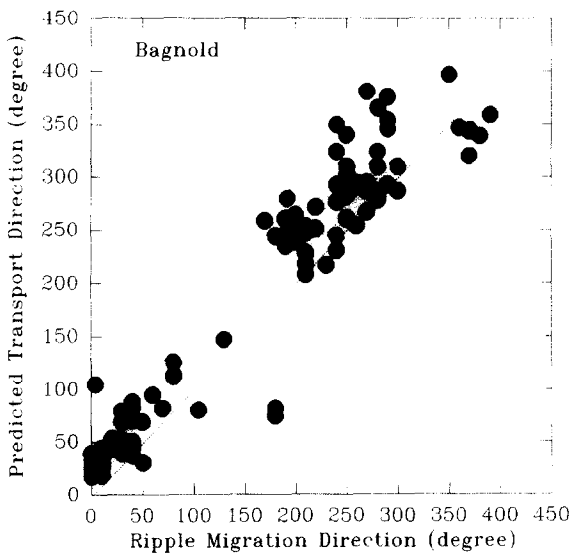

Fig. 13. The predicted mean sediment transport direction by the Bagnold total-load method plotted against the measured ripple migration direction.

the non-storm periods (days 4–6 and 23–27). These storm transport rates reached 306 and 822 kg m^{-1} day^{-1}, respectively, and are in good agreement with the 480 kg m^{-1} day^{-1} value obtained from radioactive tracer experiments for this region during the winter months (Hodgins et al., 1986). This suggests that SEDTRANS92 properly predicts the total-load sediment transport rates representing the conditions of an exposed storm-dominated continental shelf. Amos et al. (1997) find that the maximum net daily transport rate was 10–15 kg m^{-1} day^{-1} based on the 1982 summer Sable Island Bank data. These are comparable to the magnitudes during the non-storm periods of this study (days 4–6 and 20–25 in Fig. 14), which are equivalent to the summer low-energy, tide-dominated condition. During non-storm periods, currents are mostly responsible for any sediment transport. The net transport direction is determined by the peak current direction. For instance, the peak tidal current directions were 345° and 83° for days 5 and 23, respectively, the net sediment transport was thus to the north (353°) and east (92°) for these two days. Since peak tidal directions are generally to the northwest–north–northeast and southwest–south–southeast on the Sable Island Bank, net daily transport during non-storm periods is thus mostly (80%) in these directions. During storms, however, wave effects become important. The direction of net sediment transport depends on the relative directions of waves and currents at the peak of the storm. In storm one (day 2), both wave and current directions shifted from northwest to northeast during the peak of the storm. Thus the net sediment transport was to the north (356°). In the second storm (day 12), wave direction was to the northeast and steady during the whole storm duration. Though the peak current occurred at the early stage of the storm and was to the northeast (29°), the current direction changed from east to south (from 117° to 177°) at the peak of the storm. The net daily sediment transport was to the southeast (147°), following the current direction change at the peak of the storm, not that of the peak current direction at the early stage of the storm.

4. Discussion and conclusions

The field data collected from Sable Island Bank during the winter of 1992/93 provide us a valuable base to study boundary layer dynamics and sediment transport on an exposed continental shelf. The data clearly indicate that since ripples are almost always present on sandy continental shelves, it is crucial to use the enhanced combined skin-friction shear velocity at the ripple crest to determine the onset of bedload transport. Without doing so, the sediment transport frequency will be under-estimated by 70%. At high stages of sediment transport, our analyses suggest that the bedload transport roughness has to be added to the grain roughness to obtain the transport-related combined shear velocity so that the thresholds for saltation/suspension and sheet flow can be correctly determined.

The total current shear velocity and apparent bed roughness given by the GM86 model are compared to the quadratic stress law to quantify the bed stress enhancement due to wave–current interaction. We find that the total current shear velocity was enhanced 2–3 times during the storms, while the current felt an apparent bottom rough-

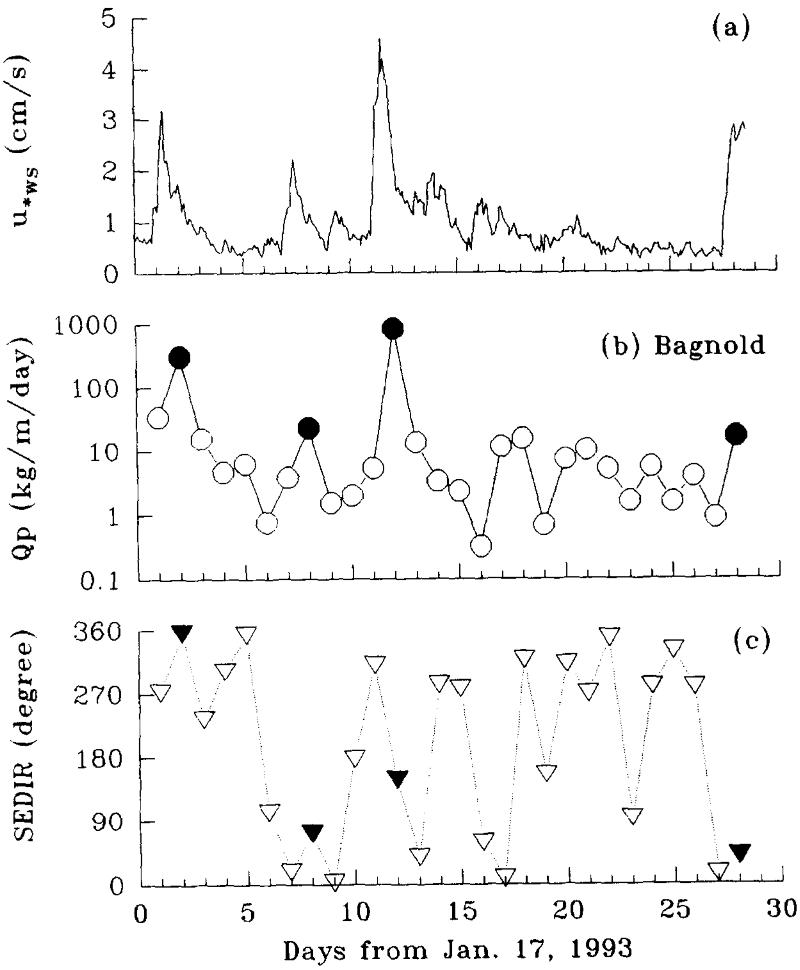

Fig. 14. Time series of (a) the skin-friction wave shear velocity, u_{*ws}, (b) net daily total sediment transport rate, and (c) sediment transport direction (SEDIR) predicted by the Bagnold total-load method. The storm events are marked by solid symbols.

ness that was more than one order of magnitude higher than that defined by the ripples and sediment grain size. The model-predicted combined skin-friction shear velocity is compared to a linearly added skin-friction shear velocity to evaluate the enhancement of combined skin-friction shear velocity due to the non-linear coupling between waves and currents inside the wave boundary layer. The results show that non-linear coupling will cause a 20% increase of the combined skin-friction shear velocity, and that this skin friction enhancement is strongest when waves and currents have roughly equal magnitudes and their angles are less than 30°.

Based on ripple migration measurements, four common unidirectional-flow sediment transport formulae are tested and evaluated for applications under combined flows. While the Engelund–Hansen total-load, Einstein–Brown bedload and Bagnold total-load formulae are all found to give reasonable predictions, the Engelund–Hansen method fails to predict any significant increase of sediment transport during storms as a total-load formula should do. Though the present study suggests that the Einstein–Brown and Bagnold methods can be used to, respectively, predict bedload and total-load sediment transport rates under combined flows, the application of the

Bagnold total-load formula (Eqs. (17a) and (17b)) is questionable as it uses the mean velocity u_{100} in the calculation and the direction of u_{100} is different from that of the combined shear velocity, u_{*cws}. The Bagnold method also uses the maximum combined skin-friction shear velocity to determine the threshold and calculate transport rate. The oscillation of waves and hence the u_{*cws} fluctuation are not considered. This is physically incorrect. It is thus recommended that if available, the correctly predicted velocity and suspended sediment concentration profiles should be used to obtain the suspended load transport and this should be added to the predicted bedload transport to obtain the total sediment transport rate. Accurate simultaneous measurements of waves, current profiles, ripple migration rates and suspended sediment concentration profiles are needed for the full test of the applicability of the Bagnold total-load formula under the combined waves and currents.

In summary, the analyses of the present data support the following conclusions:

(1) The Shields-type parameters can be applied for the determination of bedload transport initiation under combined flows, provided that the maximum enhanced shear stress at the ripple crest is used when ripples are present. Failing to do so will cause significant under-prediction of bedload sediment transport frequency.

(2) At high transport stages, a significant portion of the flow energy is spent for maintaining a bedload transport layer. This bedload roughness has to be added to the grain size roughness to compute a transport-related shear velocity which then can be used to determine the thresholds for the saltation/suspension and upper-plane bed sheet flow transports. The bedload roughness algorithms of Grant and Madsen (1982) and Wiberg and Rubin (1989) are found to under-predict under combined-flow conditions, while a modified method based on Nielsen (1992) and the data of the present study gives results that are in good agreement with the thresholds for saltation/suspension (Bagnold, 1956) and for sheet flow (Komar and Miller, 1975b).

(3) Wave–current interaction during storms enhances the total current shear velocity 2–3 times compared to current-only conditions and the bottom roughness is more than one order of magnitude higher than that defined by the sediment grain size and ripple geometry. Non-linear coupling between waves and currents also increases the skin-friction shear velocity by as much as 20% inside the wave boundary layer. This enhancement is strongest when waves and currents are approximately equal in magnitude and are separated less than 30°.

(4) Of the four unidirectional flow sediment transport formulae tested here, our data show that the Engelund–Hansen and Yalin methods do not give adequate predictions of sediment transport rates under combined waves and currents. While the Einstein–Brown bedload and Bagnold total-load methods are found to give reasonable predictions, more complete field measurements are needed for the full test of the Bagnold total-load method. The measured ripple migration direction generally agrees with that of the combined shear stress, though the predicted sediment transport directions are slightly (30°) higher than the measured directions.

(5) GSC sediment transport model SEDTRANS92 predicts that the net daily sediment transport rates can reach as high as 822 kg m^{-1} day^{-1} during storms and these are 2–3 orders of magnitude higher than that during non-storm periods. These predicted values are in good agreement with the results from sand tracer experiments conducted in this region, suggesting that SEDTRANS92 properly predicts sediment transport on an exposed, high-energy continental shelf. The net transport direction during non-storm periods on the Scotian Shelf is determined by the directions of the peak tidal currents that are mostly to the northwest–north–northeast and southwest–south–southeast. The direction of net sediment transport during storms, however, depends on the relative directions of waves and currents at the peak of the storm.

Acknowledgements

The authors would like to thank John Zevenhuizen and Bruce Wile for instrument deployment and retrieval, and Robert Courtney for help in using GRASS for seabed photo analysis. We also appreciate the co-operation of Pan Canadian (formerly LASMO Nova Scotia Ltd.) during the field work. Donald Forbes and Steve Solomon critically reviewed the manuscript of this paper. The funding for this work was provided by the Panel on Energy Research and Development (PERD) of the Federal Government of Canada through Offshore Geotechnics Program 63204. Geological Survey of Canada Contribution Number 66794.

References

Ackers, P., White, W.R., 1973. Sediment transport: new approach and analysis. J. Hydraul. Div., Proc. ASCE 99 (HY11), 2041–2060.

Allen, J.R.L., 1970. Physical Processes and Sedimentation. Unwin Univ. Books, London, 248 pp.

Amos, C.L., Judge, J.T., 1991. Sediment transport on the eastern Canadian continental shelf. Cont. Shelf Res. 11, 1068–1073.

Amos, C.L., Bowen, A.J., Huntley, D.A., Lewis, C.F.M., 1988. Ripple generation under the combined influences of waves and currents on the Canadian continental shelf. Cont. Shelf Res. 8, 1129–1153.

Amos, C.L., Bowen, A.J., Huntley, D.A., Judge, J.T., Li, M.Z., 1997. Ripple migration and sand transport under combined flows on the Scotian Shelf. Mar. Geol., submitted.

Arnott, R.W., Southard, J.B., 1990. Exploratory flow duct experiments on combined flow bed configurations and some implications for interpreting storm event stratification. J. Sediment. Petrol. 60, 211–219.

Bagnold, R.A., 1956. Flow of cohesionless grains in fluids. Philos. Trans. R. Soc. London A249, 235–297.

Bagnold, R.A., 1963. Mechanics of marine sedimentation. In: Hill, M.N. (Ed.), The Sea, Vol. 3. Wiley–Interscience, New York, pp. 507–527.

Boyd, R., Forbes, D.L., Heffler, D.E., 1988. Time-sequence observations of wave-formed sand ripples on an ocean shoreface. Sedimentology 35, 449–464.

Brown, C.B., 1950. Sediment transportation. In: Rouse, H. (Ed.), Engineering Hydraulics. Wiley, New York, p. 796.

Butman, B., Noble, M., Folger, D.W., 1979. Long-term observations of bottom current and bottom sediment movement on the Mid-Atlantic continental shelf. J. Geophys. Res. 84, 1187–1205.

Cacchione, D.A., Drake, D.E., 1990. Shelf sediment transport: an overview with applications to the Northern California continental shelf. In: LeMehaute, B., Hanes, D.M. (Eds.), The Sea, Vol. 9. Wiley–Interscience, New York, pp. 729–773.

Cacchione, D.A., Grant, W.D., Drake, D.E., Glenn, S.M., 1987. Storm-dominated bottom boundary layer dynamics on the northern California continental shelf: Measurements and predictions. J. Geophys. Res. 92, 1817–1827.

Carstens, M.R., Neilson, R.M., Altinbilek, H.D., 1969. Bedforms generated in the laboratory under oscillatory flow: analytical and experimental study. U.S. Army Corps of Engineers, Coastal Eng. Res. Cent. Tech. Mem. 28, 39

Davidson, S., Amos, C.L., 1985. A re-evaluation of SED1D and SED2D: sediment transport models for the continental shelf. Geol. Surv. Can. Open-File Rep. 1705, Sect. 3, 54 pp.

Dietrich, W.D., 1982. Flow, Boundary Shear Stress and Sediment Transport in a River Meander. Ph.D. Dissert., Univ. Washington, Seattle, 261 pp.

Dingler, J.R., Inman, D.L., 1976. Wave-formed ripples in nearshore sands. Proc. 15th Coastal Eng. Conf., ASCE, New York, pp. 2109–2126.

Drake, D.E., Cacchione, D.A., 1986. Field observations of bed shear stress and sediment resuspension on continental shelves, Alaska and California. Cont. Shelf Res. 6, 415–429.

Drake, D.E., Cacchione, D.A., 1992. Wave-current interaction in the bottom boundary layer during storm and non-storm conditions: observations and model predictions. Cont. Shelf Res. 12, 1331–1352.

Du Toit, C.G., Sleath, J.F.A., 1981. Velocity measurements close to rippled beds in oscillatory flow. J. Fluid Mech. 112, 71–96.

Engelund, F., Hansen, E., 1967. A monograph on sediment transport in alluvial streams. Teknisk Vorlag, Copenhagen, 62 pp.

Gadd, P.E., Lavelle, J.W., Swift, D.J.P., 1978. Estimate of sand transport on the New York shelf using near-bottom current meter observations. J. Sediment. Petrol. 48, 239–252.

Gibbs, R.J., Mathews, M.D., Link, D.A., 1971. The relationship between sphere size and settling velocity. J. Sediment. Petrol. 41, 7–18.

Glenn, S.M., Grant, W.D., 1987. A suspended sediment stratification correction for combined wave and current flows. J. Geophys. Res. 92, 8244–8264.

Grant, W.D., Madsen, O.S., 1979. Combined wave and current interaction with a rough bottom. J. Geophys. Res. 84, 1797–1808.

Grant, W.D., Madsen, O.S., 1982. Moveable bed roughness in unsteady oscillatory flow. J. Geophys. Res. 87, 469–481.

Grant, W.D., Madsen, O.S., 1986. The continental shelf bottom boundary layer. Annu. Rev. Fluid Mech. 18, 265–305.

Grant, W.D., Williams, A.J., Glenn, S.M., 1984. Bottom stress estimates and their prediction on the northern California continental shelf during CODE-1: The importance of wave–current interaction. J. Phys. Oceanogr. 14, 506–527.

Green, M.O., Rees, J.M., Pearson, N.D., 1990. Evidence for the influence of wave–current interaction in a tidal boundary layer. J. Geophys. Res. 95, 9629–9644.

Guy, H.P., Simons, D.B., Richardson, E.V., 1966. Summary of alluvial channel data from flume experiments, 1956–1961. U.S. Geol. Surv. Prof. Pap. 462-I, Washington, D.C., 96 pp.

Hammond, T.M., Collins, M.B., 1979. On the threshold of transport of sand-sized sediment under the combined influence of unidirectional and oscillatory flow. Sedimentology 26, 795–812.

Heathershaw, A.D., 1981. Comparisons of measured and predicted sediment transport rates in tidal currents. In: Nittrouer, C.A. (Ed.), Sedimentary Dynamics of Continental Shelves. Mar. Geol. 42, 75–104.

Heffler, D.E., 1984. RALPH—An instrument to monitor seabed sediments. Current Res. Part B, Geol. Surv. Can. Pap. 84-1b, 47–52.

Hodgins, D.O., Sayao, O.J., 1986. Field measurements of sediment transport on the Scotian Shelf, Vol. II. Boundary layer measurements and sand transport prediction. Environmental Studies Revolving Funds, Rep. 041, Ottawa, 114 pp.

Hodgins, D.O., Drapeau, G., King, L.H., 1986. Field measurements of sediment transport on the Scotian Shelf, Vol. I. The radio-isotope experiment. Environmental Studies Revolving Funds, Rep. 041, Ottawa, 160 pp.

Huntley, D.A., Hazen, D.G., 1988. Seabed stresses in combined wave and steady flow conditions on the Nova Scotia continental shelf: Field measurements and predictions. J. Phys. Oceanogr. 18, 347–362.

Inman, D.L., 1957. Wave-generated ripples in nearshore sands. U.S. Army Corps of Engineers, Beach Erosion Board, Washington, D.C., Tech. Mem. 100, 66 pp.

Kachel, N.B., Sternberg, R.W., 1971. Transport of bedload as ripples during an ebb current. Mar. Geol. 10, 229–244.

Kapdasli, M.S., 1990. Threshold condition of sand particles under codirectional combined wave and current flow. Geo-Mar. Lett. 10, 45–49.

Kapdasli, M.S., Dyer, K.R., 1986. Threshold conditions for sand movement on a rippled bed. Geo-Mar. Lett. 6, 161–164.

Komar, P.D., Miller, M.C., 1975a. On the comparison between the threshold of sediment motion under waves and unidirectional currents with a discussion of the practical evaluation of the threshold. J. Sediment. Petrol. 45, 362–367.

Komar, P.D., Miller, M.C., 1975b. The initiation of oscillatory ripple marks and the development of plane-bed at high shear stresses under waves. J. Sediment. Petrol. 45, 697–703.

Larsen, L.H., Sternberg, R.W., Shi, N.C., Marsden, M.A.H., Thomas, L., 1981. Field investigations of the threshold of grain motion by ocean waves and currents. Mar. Geol. 42, 105–132.

Lees, B.J., 1983. A relationship of sediment transport rates and paths to sandbanks in a tidally dominated area off the coast of East Anglia, U.K.. Sedimentology 30, 461–483.

Li, M.Z., 1994. Direct skin friction measurements and stress partitioning over movable sand ripples. J. Geophys. Res. 99, 791–799.

Li, M.Z., Amos, C.L., 1995. SEDTRANS92: A sediment transport model for continental shelves. Comput. Geosci. 21, 533–554.

Li, M.Z., Amos, C.L., 1997. Predicting ripple geometry and bed roughness under combined waves and currents in a continental shelf environment. Cont. Shelf Res., in press.

Li, Z., Komar, P.D., 1986. Laboratory measurements of pivoting angles for applications to selective entrainment of gravel in a current. Sedimentology 33, 413–423.

Li, M.Z., Wright, L.D., Amos, C.L., 1996. Predicting ripple roughness and sand resuspension under combined flows in a shoreface environment. Mar. Geol. 130, 139–161.

Madsen, O.S., Grant, W.D., 1975. The threshold of sediment movement under oscillatory waves: a discussion. J. Sediment. Petrol. 45, 360–361.

Manohar, M., 1955. Mechanics of bottom sediment movement due to wave action. U.S. Army Corps of Engineers, Beach Erosion Board, Washington, D.C., Tech. Mem. 75, 121 pp.

Martec Ltd., 1984. SED1D: A sediment transport model for the continental shelf. Unpubl. Rep. Submitted to the Geol. Surv. Can., DSS Contract IOSC. 23420-3-M753, 63 pp.

Martec Ltd., 1987. Upgrading of AGC sediment transport model. Geol. Surv. Can., Open-File Rep. 1705, Sect. 10 C, 14 pp.

Miller, M.C., Komar, P.D., 1980a. Oscillation sand ripples generated by laboratory apparatus. J. Sediment. Petrol. 50, 173–182.

Miller, M.C., Komar, P.D., 1980b. A field investigation of the relationship between oscillation ripple spacing and the near-bottom water orbital motion. J. Sediment. Petrol. 50, 183–191.

Miller, M.C., McCave, I.N., Komar, P.D., 1977. Threshold of sediment motion under unidirectional currents. Sedimentology 24, 507–527.

Miller, R.L., Byrne, R.J., 1966. The angle of repose for a single grain on a fixed rough bed. Sedimentology 6, 303–314.

Mobil Oil Canada Ltd., 1983. Venture development project environmental impact statement, Vol. IIa, Biophysical assessment. Mobil Oil Canada Ltd., Submitted to Canada Oil and Gas Lands Administration, Ottawa, 415 pp.

Mogridge, G.R., Kamphuis, J.W., 1972. Experiments on bedform generation by wave action. Proc. 13th Coastal Eng. Conf., ASCE, Vancouver, pp. 1123–1142.

Mogridge, G.R., Davies, M.H., Willis, D.H., 1994. Geometry prediction for wave-generated bedforms. Coastal Eng. 22, 255–286.

Nielsen, P., 1981. Dynamics and geometry of wave-generated ripples. J. Geophys. Res. 86, 6467–6472.

Nielsen, P., 1986. Suspended sediment concentrations under waves. Coastal Eng. 10, 23–31.

Nielsen, P., 1992. Coastal bottom boundary layers and sediment transport. Advanced Series on Ocean Eng., Vol. 4. World Scientific, Singapore, 324 pp.

Paola, C., 1983. Flow and skin friction over natural rough beds. Sc.D. Dissert., MIT–WHOI Jt. Prog. Oceanogr., Mass. Inst. of Technol./Woods Hole Oceanogr. Inst., Woods Hole, MA, 338 pp.

Pattiaratchi, C.B., Collins, M.B., 1984. Sediment transport under waves and tidal currents: a case study from the northern Bristol Channel, U.K. Mar. Geol. 56, 27–40.

Pattiaratchi, C.B., Collins, M.B., 1985. Sand transport under the combined influence of waves and tidal currents: An assessment of available formulae. Mar. Geol. 67, 83–100.

Sawamoto, M., Yamashita, T., 1986. Sediment transport rate due to wave action. J. Hydrosci. Hydraul. Eng. 4, 1–15.

Smith, J.D., 1977. Modelling of sediment transport on continental shelves. In: Goldberg, E.D. et al. (Eds.), The Sea, Vol. 6. Wiley–Interscience, New York, pp. 539–577.

Smith, J.D., Hopkins, T.S., 1972. Sediment transport on the continental shelf off of Washington and Oregon in light of recent current measurements. In: Swift, D.J.P., Duane, D.B., Pilkey, O.H. (Eds.), Shelf Sediment Transport: Process and Pattern. Dowden, Hutchinson and Ross, Stroudsburg, PA, pp. 143–180.

Smith, J.D., McLean, S.R., 1977. Boundary layer adjustments to bottom topography and suspended sediments. In: Nihoul, J.C.J. (Ed.), Bottom Turbulence. Elsevier, New York, pp. 123–151.

Soulsby, R.L., 1983. The bottom boundary layer of shelf seas. In: Johns, B. (Ed.), Physical Oceanography of Coastal and Shelf Seas. Elsevier, Amsterdam, Ch. 5.

Sternberg, R.W., 1972. Predicting initial motion and bedload transport of sediment particles in the shallow marine environment. In: Swift, D.J.P., Duane, D.B., Pilkey, O.H. (Eds.), Shelf Sediment Transport: Process and Pattern. Dowden, Hutchinson and Ross, Stroudsburg, PA, pp. 61–82.

Swart, D.H., 1974. Offshore sediment transport and equilibrium beach profiles. Delft Hydraul. Lab. Publ. 131.

Swift, D.J.P., Han, G., Vincent, C.E., 1986a. Fluid processes and sea-floor response on a modern storm-dominated shelf: Middle Atlantic shelf of North America, Part I. The storm current regime. In: Knight, R.J., McLean, J.R. (Eds.), Shelf Sands and Sandstones. Can. Soc. Pet. Geol., Mem. II, Calgary, pp. 99–120.

Swift, D.J.P., Thorne, J., Oertel, G.F., 1986b. Fluid processes and sea-floor response on a modern storm-dominated shelf: Middle Atlantic shelf of North America, Part II. Response of the Shelf Floor. In: Knight, R.J., McLean, J.R. (Eds.), Shelf Sands and Sandstones. Can. Soc. Pet. Geol., Mem. II, Calgary, pp. 191–212.

Vincent, C.E., Hanes, D.M., Bowen, A.J., 1991. Acoustic measurements of suspended sand on the shoreface and the control of concentration by bed roughness. Mar. Geol. 96, 1–18.

White, W.R., Milli, H., Grabbe, A.D., 1975. Sediment transport theories: a review. Proc. Inst. Civ. Eng. 59, 265–292.

Wiberg, P.L., Harris, C.K., 1994. Ripple geometry in wave-dominated environments. J. Geophys. Res. 99, 775–789.

Wiberg, P.L., Nelson, J.M., 1992. Unidirectional flow over asymmetric and symmetric ripples. J. Geophys. Res. 97, 12745–12761.

Wiberg, P.L., Rubin, D.M., 1989. Bed roughness produced by saltating sediment. J. Geophys. Res. 94, 5011–5016.

Wilson, K.C., 1966. Bed-load transport at high shear stress. J. Hydraul. Div., ASCE 92 (HY6), 49–59.

Wilson, K.C., 1988. Mobile-bed friction at high shear stress. J. Hydraul. Eng., ASCE 115, 825–830.

Yalin, M.S., 1963. An expression for bedload transportation. J. Hydraul. Div., Proc. ASCE 89 (HY3), 221–250.

Yalin, M.S., 1977. Mechanics of Sediment Transport. Pergamon, Oxford, 298 pp.

Yalin, M.S., Karahan, E., 1979. Inception of sediment transport. J. Hydraul. Div., Am. Soc. Civ. Eng. 105, 1433–1443.